BULLETIN OF THE EARTHQUAKE
RESEARCH INSTITUTE
Vol. 45 (1967), pp. 601-624

33. *Theoretical Seismograms of Spheroidal Type on the Surface of a Gravitating Elastic Sphere.*

II. Case of Gutenberg-Bullen A′ Earth Model.

By Yasuo SATÔ, Tatsuo USAMI

Earthquake Research Institute

and

Mark LANDISMAN,

Geosciences Division, Southwest Center for Advanced Studies.

(Read June 27, 1967.—Received June 30, 1967.)

1. Introduction

Calculations for a homogeneous elastic sphere were reported in the first study of theoretical seismograms illustrating the effects of gravity on the propagation of spheroidal disturbances[1]. In this investigation it was found that the influence of gravity on the non-dimensional frequency is large for modes with periods longer than 200 seconds and decreases rapidly with increasing frequency, becoming negligible for shorter periods. The resulting theoretical seismograms, however, did not greatly differ from those calculated for the corresponding case excluding the effect of gravity[2].

The present study, the second investigation of the effect of gravity on the periods of the free oscillation, its effects on the phase and group velocities, common spectrum and on the resulting theoretical seismograms, is an important part of our continuing program of investigation of the generation, propagation, dispersion and attenuation of seismic waves in realistic spherical earth models[3)–5)]. The theoretical seismograms reported

(Contribution No. 57 Geosciences Division, Southwest Center for Advanced Studies.)

1) T. USAMI and Y. SATÔ, "Theoretical Seismogram of Spheroidal Type on the Surface of a Homogeneous Gravitating Spherical Earth", *Bull. Earthq. Res. Inst.*, **44** (1966), 779-791.

2) T. USAMI and Y. SATÔ, "Propagation of Spheroidal Disturbances on a Homogeneous Elastic Sphere", *Bull. Earthq. Res. Inst.*, **42** (1964), 273-287.

3) T. USAMI, Y. SATÔ and M. LANDISMAN, "Preliminary Study of the Propagation of Spheroidal Disturbances on the Surface of a Heterogeneous Spherical Earth", *Geophys. J.*, **11** (1965), 243-251.

here, which represent disturbances on the surface of a Gutenberg-Bullen A′ earth model, were calculated by summing the contributions from the free spheroidal oscillations through the tenth radial mode, for all orders from the gravest with periods near 50 minutes to those with periods near 80 sec. Radial distributions of displacement, phase and group velocities, the common spectrum and theoretical seismograms were calculated and comparisons were made with the corresponding quantities found for the case without gravity[3)-4)].

Notable results of the study of the propagation of spheroidal disturbances on the surface of a Gutenberg-Bullen A′ earth model, when the effect of gravity is considered, are:

1. The difference of non-dimensional frequency between the present case and the case which excludes the effect of gravity is a rather complicated function of the order number n and the radial mode number i. The discrepancy is large for modes lying along the special transition segments between each radial mode and the next higher one; it tends toward negligible values as the order number increases.

2. The corresponding phase and group velocities exhibit their greatest differences for the first three radial modes and for orders less than about 15. The maximum group velocity for the radial mode $i=3$, which is associated with the R_h wave[4)], is larger when the effect of gravity is included. The present calculations indicate that gravity does not influence the period and velocity of the waves corresponding to the fundamental mode group velocity minimum.

3. The radial distributions of displacement show that there is little difference between the two cases except for certain modes which move to a branch of different character.

4. The common spectrum does not exhibit any great difference between the two cases.

5. There is no difference in the theoretical seismograms initially following the occurrence of the disturbance, but the discrepancy caused by the introduction of gravity becomes increasingly large as time progresses. A short period wave suddenly becomes predominant near the antipode.

---

4) T. USAMI, Y. SATÔ and M. LANDISMAN, "Theoretical Seismograms of Spheroidal Type on the Surface of a Heterogeneous Spherical Earth", *Bull. Earthq. Res. Inst.*, **43** (1965), 641-660.

5) T. USAMI, Y. SATÔ and M. LANDISMAN, "Theoretical Seismograms of Torsional Disturbances Excited at a Focus Within a Heterogeneous Spherical Earth — Case of a Gutenberg-Bullen A′ Earth Model —", *Bull. Seism. Soc. Amer.*, in press.

2. Glossary

Case (I) : The problem of a non-gravitating sphere[4]
Case (II): The problem of a gravitating sphere
a: radius of the earth
b: radius of the core
C, U: phase and group velocities
E_S, E_T: radial and colatitudinal stress on the earth's surface
$f(t)$: time function of the external force
$f^*(p)$: Fourier transform of the function $f(t)$
g_0: gravity in the undisturbed state
i: radial mode number
j: unit of the imaginary number
k: $(=p/V_{SO})$
m: degree of an associated Legendre function (azimuthal mode number)
n: order of an associated Legendre function (colatitudinal mode number)
${}_ip_n$: circular frequency of free oscillation
P_{diffr}: P wave diffracted into the shadow zone by the core
$P_n^m(\cos\theta)$: associated Legendre function by Ferrers' definition
(r, θ, φ): polar coordinates
${}_iS_n^u$, ${}_iS_n^v$: common spectrum of radial and colatitudinal components of disturbance
S_{mn}, T_{mn}: coefficients of spherical surface harmonics in the expansion of radial and colatitudinal components of applied force
t: time
(u, v, w): displacement in the r-, θ- and φ-directions
$U_n(r)$, $V_n(r)$: function giving the radial distribution of u and v
${}_iu_n$, ${}_iv_n$: contribution of a normal mode oscillation for the radial mode number i and the order number n
$({}_iu_n)$, $({}_iv_n)$: $\sum_{i'=1}^{i}\sum_{n'=0}^{n} {}_{i'}u_{n'}$; $\sum_{i'=1}^{i}\sum_{n'=0}^{n} {}_{i'}v_{n'}$
$[{}_iu_n]$, $[{}_iv_n]$: $\sum_{n'=0}^{n} {}_iu_{n'}$; $\sum_{n'=0}^{n} {}_iv_{n'}$
V_P, V_S: velocities of dilatational and shear waves
V_{SO}: S wave velocity on the surface of the earth
$Y_n(r)$: function giving the radial distribution of ψ
α: ratio of the colatitudinal to the radial component of displacement of the surface

β: value of the gravity potential on the surface of the earth
γ: universal gravitational constant
η: non-dimensional frequency of free oscillation ($=ka=pa/V_{so}$)
λ, μ: Lamé's elastic moduli
ρ_0: density in the undisturbed state
ψ: gravity potential due to disturbances
$\Phi(\theta, \varphi)$: geographical distribution of external force ($=\Phi^0(\cos\theta)$ in the present case)

3. Fundamental Expressions

The spheroidal disturbances of a radially heterogeneous elastic sphere may be expressed in terms of the polar coordinates (r, θ, φ). When the effect of gravity is considered, these expressions are

$$(u, v, w, \psi)=\frac{1}{2\pi}\int_{-\infty}^{\infty}(u(p), v(p), w(p), \psi(p))\cdot\exp(jpt)dp\ , \tag{3.1}$$

$$\left.\begin{aligned}
u(p)&=\sum_{m,n}A_{mn}\cdot U_n(r)\cdot P_n^m(\cos\theta)\cdot\begin{matrix}\cos\\ \sin\end{matrix} m\varphi\cdot f^*(p)\ ,\\
v(p)&=\sum_{m,n}A_{mn}\cdot V_n(r)\cdot\frac{d}{d\theta}P_n^m(\cos\theta)\cdot\begin{matrix}\cos\\ \sin\end{matrix} m\varphi\cdot f^*(p)\ ,\\
w(p)&=\sum_{m,n}m\cdot A_{mn}\cdot V_n(r)\cdot\frac{P_n^m(\cos\theta)}{\sin\theta}\cdot\begin{matrix}-\sin\\ \cos\end{matrix} m\varphi\cdot f^*(p)\ ,\\
\psi(p)&=\sum_{m,n}A_{mn}\cdot Y_n(r)\cdot P_n^m(\cos\theta)\cdot\begin{matrix}\cos\\ \sin\end{matrix} m\varphi\cdot f^*(p)\ .
\end{aligned}\right\} \tag{3.2}$$

where u, v, w are the displacement components in the r-, θ-, φ-directions and ψ is the gravity potential due to the disturbances. U_n, V_n, and Y_n satisfy the simultaneous differential equations,

$$\left.\begin{aligned}
&\frac{d}{dr}(\lambda X_n+2\mu\dot{U}_n)+\frac{\mu}{r^2}[4r\dot{U}_n-4U_n+n(n+1)(-U_n-r\dot{V}_n+3V_n)]\\
&\qquad+\rho_0\dot{Y}_n+\rho_0 g_0 X_n-\rho_0\frac{d}{dr}(g_0U_n)+\rho_0 p^2U_n=0\ ,\\
&\frac{d}{dr}\left[\mu\left(\dot{V}_n-\frac{V_n-U_n}{r}\right)\right]+\frac{\mu}{r^2}[5U_n+3r\dot{V}_n-V_n-2n(n+1)V_n]\\
&\qquad+\frac{\lambda}{r}X_n+\frac{\rho_0}{r}Y_n-\frac{\rho_0 g_0}{r}U_n+\rho_0 p^2V_n=0\ ,
\end{aligned}\right\} \tag{3.3}$$

$$\left.\begin{aligned}
&\dot{Y}_n+\frac{2}{r}\dot{Y}_n-\frac{n(n+1)}{r^2}Y_n=4\pi\gamma(\dot{\rho}_0U_n+\rho_0X_n)\ ,\\
&X_n=\dot{U}_n+\frac{2}{r}U_n-\frac{n(n+1)}{r}V_n\ .
\end{aligned}\right\}$$

As noted in § 2, γ is the universal constant of gravitation and ρ_0 and g_0 are the density and gravity in the undisturbed state. A dot over a quantity implies differentiation with respect to the radius r. Equations (3.3) may be reduced to a form convenient for numerical integration,

$$\left.\begin{aligned}
&\frac{\lambda+2\mu}{\rho_0}U_n''+MU_n'+NV_n'+LV_n+(\rho_0^2a^2+K)U_n+JY_n'=0\ ,\\
&\frac{\mu}{\rho_0}V_n''+\bar{M}V_n'+\bar{N}U_n'+\bar{L}U_n+(\rho_0^2a^2+\bar{K})V_n+\bar{J}Y_n=0\ ,\\
&Y_n''+\frac{2}{\zeta}Y_n'-\frac{n(n+1)}{\zeta^2}Y_n=4\pi a\gamma\left[(\rho_0U_n)'+\frac{2\rho_0U_n}{\zeta}-\frac{n(n+1)\rho_0}{\zeta}V_n\right].
\end{aligned}\right\}\tag{3.4}$$

where the dash implies differentiation with respect to the dimensionless radius $\zeta=r/a$. The coefficients in (3.4) are

$$\left.\begin{aligned}
M&=(\lambda'+2\mu')/\rho_0+2(\lambda+2\mu)/\rho_0\zeta\ ,\\
N&=-n(n+1)(\lambda+\mu)/\rho_0\zeta\ ,\\
L&=n(n+1)[(\lambda+3\mu)/\rho_0\zeta^2-\lambda'/\rho_0\zeta-ag_0/\zeta]\ ,\\
K&=2\lambda'/\rho_0\zeta-[2(\lambda+2\mu)+n(n+1)\mu]/\rho_0\zeta^2+2g_0a/\zeta-ag_0'\ ,\\
J&=a\ ,\\
\bar{M}&=\mu'/\rho_0+2\mu/\rho_0\zeta\ ,\\
\bar{N}&=(\lambda+\mu)/\rho_0\zeta\ ,\\
\bar{L}&=\mu'/\rho_0\zeta+2(\lambda+2\mu)/\rho_0\zeta^2-ag_0/\zeta\ ,\\
\bar{K}&=-\mu'/\rho_0\zeta-n(n+1)(\lambda+2\mu)/\rho_0\zeta^2\ ,\\
\bar{J}&=a/\zeta\ .
\end{aligned}\right\}\tag{3.5}$$

In a liquid media, too, the equations (3.4) and (3.5) are valid provided that $\mu=\mu'=0$. Since no torsional motion can exist within a liquid, the

equation system (3.4) may be reduced to two independent equations for the two unknown quantities, U_n and Y_n without difficulty. They are

$$\left.\begin{aligned} &AU_n''+BU_n'+CU_n+DY_n'+EY_n=0\ , \\ &Y_n''+\bar{B}Y_n'+\bar{C}Y_n+\bar{D}U_n'+\bar{E}U_n=0. \end{aligned}\right\} \tag{3.6}$$

where

$$\left.\begin{aligned} &A=\lambda p^2a^2/\rho_0Q\ , \\ &B=M+\frac{n(n+1)\lambda}{\rho_0\zeta Q^2}\left[\frac{p^2a^2}{\zeta}\left(\left(\frac{\lambda}{\rho_0}\right)'+\frac{\lambda'}{\rho_0}\right)-\frac{n(n+1)}{\zeta^2}\left(\frac{2\lambda^2}{\rho_0^2\zeta^2}+\frac{\lambda\lambda'}{\rho_0^2\zeta}\right)\right], \\ &C=p^2a^2+K-\frac{n(n+1)}{\zeta Q^2}\left[p^2a^2\left\{\frac{\lambda ag_0'}{\rho_0\zeta}+\frac{6\lambda^2}{\rho_0^2\zeta^3}+\frac{2\lambda^2\rho_0'}{\rho_0^3\zeta^2}+\left(ag_0-\frac{4\lambda}{\rho_0\zeta}\right)\left(\frac{ag_0}{\zeta}+\frac{\lambda'}{\rho_0\zeta}\right)\right\}\right. \\ &\qquad\left.-\frac{n(n+1)\lambda}{\rho_0\zeta^3}\left\{\frac{\lambda ag_0'}{\rho_0}-\frac{2\lambda ag_0}{\rho_0\zeta}-\frac{2\lambda\lambda'}{\rho_0^2\zeta}+\frac{2\lambda^2}{\rho_0^2\zeta^2}+(ag_0)^2+\frac{ag_0\lambda\rho_0'}{\rho_0^2}\right\}\right], \\ &D=p^2a^3/Q\ , \\ &E=-\frac{n(n+1)a}{\zeta Q^2}\left[p^2a^2\left(\frac{2\lambda}{\rho_0\zeta^2}-\frac{\lambda'}{\rho_0\zeta}-\frac{ag_0}{\zeta}\right)+\frac{n(n+1)\lambda}{\rho_0\zeta}\left(\frac{ag_0}{\zeta^2}+\frac{\lambda\rho_0'}{\rho_0^2\zeta^2}\right)\right], \\ &\bar{B}=2/\zeta\ , \\ &\bar{C}=-n(n+1)(4\pi a\gamma\rho_0\bar{J}/Q\zeta+1/\zeta^2)\ , \\ &\bar{D}=-4\pi a\gamma\rho_0\cdot p^2a^2/Q\ , \\ &\bar{E}=-4\pi a\gamma[\rho_0'+\rho_0(2p^2a^2-n(n+1)ag_0/\zeta)/\zeta Q]\ , \\ &Q=p^2a^2-n(n+1)\lambda/\rho_0\zeta^2\ . \end{aligned}\right\} \tag{3.7}$$

Values of $V_n(\zeta)$ may be obtained from U_n and Y_n by means of either the second equation of (3.4) or the equation derived by eliminating V_n'' and V_n' from the first and second equations of (3.4).

At a boundary between two different media, the values of U_n, V_n and Y_n and their derivatives with regard to ζ may be obtained from the corresponding values for the other medium by means of the boundary conditions. These conditions are

$$\left.\begin{aligned} &(U_n)_1=(U_n)_2\ , \\ &(V_n)_1=(V_n)_2\ , \end{aligned}\right.$$

$$\left.\begin{aligned}
&\left[(\lambda+2\mu)U'_n+\frac{2\lambda}{\zeta}U_n-\frac{n(n+1)}{\zeta}\lambda V_n\right]_1=\left[(\lambda+2\mu)U'_n+\frac{2\lambda}{\zeta}U_n-\frac{n(n+1)}{\zeta}\lambda V_n\right]_2,\\
&\left[\mu\left(V'_n-\frac{V_n-U_n}{\zeta}\right)\right]_1=\left[\mu\left(V'_n-\frac{V_n-U_n}{\zeta}\right)\right]_2,\\
&(Y_n)_1=(Y_n)_2,\\
&[Y'_n-4\pi\gamma a\rho_0 U_n]_1=[Y'_n-4\pi a\gamma\rho_0 U_n]_2.
\end{aligned}\right\} \tag{3.8}$$

When the core is liquid, one of the boundary conditions at the core-mantle boundary assuring the continuity of the colatitudinal displacement V_n disappears and the condition of the continuity of the colatitudinal stress component gives no effective means to determine the initial values for the core. Supposing that simultaneous equations (3.4) are numerically integrated from the surface towards the center, the value of $(U'_n)_{r=b}$ for the core may be calculated by solving the third equation of (3.8) and the second equation of (3.4), μ and μ' being put to zero, for two unknowns $(U'_n)_{r=b}$ and $(V_n)_{r=b}$ of the core.

The displacement components in the time domain can be obtained from (3.1) by the technique of Fourier transformation

$$\left.\begin{aligned}
u&=\frac{1}{2\pi}\sum_{m,n}P_n^m(\cos\theta)\cdot\begin{matrix}\cos\\ \sin\end{matrix}m\varphi\cdot\int_{-\infty}^{\infty}\left(\frac{S_{mn}}{E_S}+\frac{T_{mn}}{E_T}\right)\\
&\qquad\times U_n(r)\cdot f^*(p)\cdot\exp(jpt)\cdot dp,\\
v&=\frac{1}{2\pi}\sum_{m,n}\frac{d}{d\theta}P_n^m(\cos\theta)\cdot\begin{matrix}\cos\\ \sin\end{matrix}m\varphi\cdot\int_{-\infty}^{\infty}\left(\frac{S_{mn}}{E_S}+\frac{T_{mn}}{E_T}\right)\\
&\qquad\times V_n(r)\cdot f^*(p)\cdot\exp(jpt)\cdot dp,\\
w&=\frac{1}{2\pi}\sum_{m,n}m\frac{P_n^m(\cos\theta)}{\sin\theta}\cdot\begin{matrix}-\sin\\ \cos\end{matrix}m\varphi\cdot\int_{-\infty}^{\infty}\left(\frac{S_{mn}}{E_S}+\frac{T_{mn}}{E_T}\right)\\
&\qquad\times V_n(r)\cdot f^*(p)\cdot\exp(jpt)\cdot dp.
\end{aligned}\right\} \tag{3.9}$$

In these expressions, S_{mn} and T_{mn} are the coefficients of the spherical surface harmonics in the longitudinal and colatitudinal expansion of the radial and tangential stresses applied on the surface of the elastic sphere. E_S and E_T, the radial and tangential stress at the free surface $r=a$, are written as

$$E_S=(\lambda+2\mu)_a\cdot\dot{U}_n(a)+\frac{(\lambda)_a}{a}\cdot(2U_n(a)-n(n+1)V_n(a)), \tag{3.10}$$

$$E_T=(\mu)_a\cdot\left(\dot{V}_n(a)-\frac{1}{a}(V_n(a)-U_n(a))\right) . \tag{3.10}$$

$E_S=E_T=0$, together with the equation

$$\dot{Y}_n(a)+\frac{n+1}{a}Y_n(a)=4\pi\gamma\cdot(\rho_0)_a\cdot U_n(a) , \tag{3.11}$$

give the surface conditions of the free spheroidal oscillations of a gravitating elastic sphere.

Equations (3.9) were evaluated by contour integration which showed that the disturbances can be represented by superposition of the contributions from the poles corresponding to the free oscillations

$$\left.\begin{aligned}
u(t) &= \frac{j}{2}\sum_{i,m,n}P_n^m(\cos\theta)\cdot\begin{matrix}\cos\\ \sin\end{matrix} m\varphi\cdot\left[\left(\frac{S_{mn}}{dE_S/dp}+\frac{T_{mn}}{dE_T/dp}\right)\right.\\
&\qquad\left.\times U_n(r)\cdot f^*(p)\cdot\exp(jpt)\right]_{p={}_ip_n} ,\\
v(t) &= \frac{j}{2}\sum_{i,m,n}\frac{d}{d\theta}P_n^m(\cos\theta)\cdot\begin{matrix}\cos\\ \sin\end{matrix} m\varphi\cdot\left[\left(\frac{S_{mn}}{dE_S/dp}+\frac{T_{mn}}{dE_T/dp}\right)\right.\\
&\qquad\left.\times V_n(r)\cdot f^*(p)\cdot\exp(jpt)\right]_{p={}_ip_n} ,\\
w(t) &= \frac{j}{2}\sum_{i,m,n}\frac{mP_n^m(\cos\theta)}{\sin\theta}\cdot\begin{matrix}-\sin\\ \cos\end{matrix} m\varphi\cdot\left[\left(\frac{S_{mn}}{dE_S/dp}+\frac{T_{mn}}{dE_T/dp}\right)\right.\\
&\qquad\left.\times V_n(r)\cdot f^*(p)\cdot\exp(jpt)\right]_{p={}_ip_n} .
\end{aligned}\right\} \tag{3.12}$$

In this formula ${}_ip_n$ are the frequencies of the free spheroidal oscillation of the gravitating earth. In the present study, a purely radial stress was assumed to act on the surface in a small circle around the pole. In this case, $m=0$, $T_{mn}=0$ and the azimuthal component of disturbance, w, is identically zero.

4. Earth Model

A detailed explanation of the Gutenberg-Bullen A′ model used in the present study was presented in our previous paper[3]. Except for trivial modifications, the model follows Gutenberg's distribution of the velocities of compressional and shear waves and Bullen's A′ distribution of density. The radial variation of P and S velocities and of density

appear in both graphical and tabular form in an earlier report[4].

5. Non-dimensional Frequency

The non-dimensional frequency $\eta\,(=ka=pa/V_{so})$ of spheroidal oscillations of the earth was calculated by numerically integrating the simultaneous equations (3.4), under the conditions of zero stress and continuity of gravity potential on the surface. The integration was executed from the surface towards the center, assuming the radial displacement on the surface to be 1.

The solutions to the problem of free spheroidal oscillation in a radially heterogeneous sphere were found for the non-gravitating case by a two-dimensional search for the two unknown quantities, namely, η, the dimensionless eigenfrequency, and α, the surface ratio of displacement $(=nV_n/U_n)$. In the present case, however, the surface value of the gravity potential β enters as a third unknown and the problem of determining the free oscillations is solved by a three-dimensional search for the unknown quantities η, α and β. Test criteria for the search are the vanishing of the tangential stress at the bottom of the mantle and the vanishing of the displacements and gravity potential at great depth. The actual search for the unknown quantities was performed in the order α, β and η. The search process employed in the present investigation is similar to that adopted for case (I), which is described in the corresponding report[4].

The values of dE_s/dp, which are necessary for evaluating the contributions of each mode, were computed in a manner similar to that used for the torsional problem[6].

Non-dimensional frequencies of free spheroidal oscillations were calculated for vibrations with periods longer than about 80 seconds corresponding to the first ten radial modes.

Curves of dimensionless eigenfrequency vs. order number n are presented in Figure 1a. For comparison, the frequencies for case (I) are shown in the illustration as broken lines. In order to show the discrepancy between cases (I) and (II), the low-frequency portion of

6) Y. SATÔ, T. USAMI, M. LANDISMAN and M. EWING, "Basic Study on the Oscillation of a Sphere Part V: Propagation of Torsional Disturbances on a Radially Heterogeneous Sphere. Case of a Homogeneous Mantle with a Liquid Core", *Geophys. J.*, **8** (1963), 44-63.

7) Y. SATÔ and T. USAMI, "Basic Study on the Oscillation of a Homogeneous Elastic Sphere. II. Displacement Distribution", *Geophys. Mag.*, **31** (1962), 25-47.

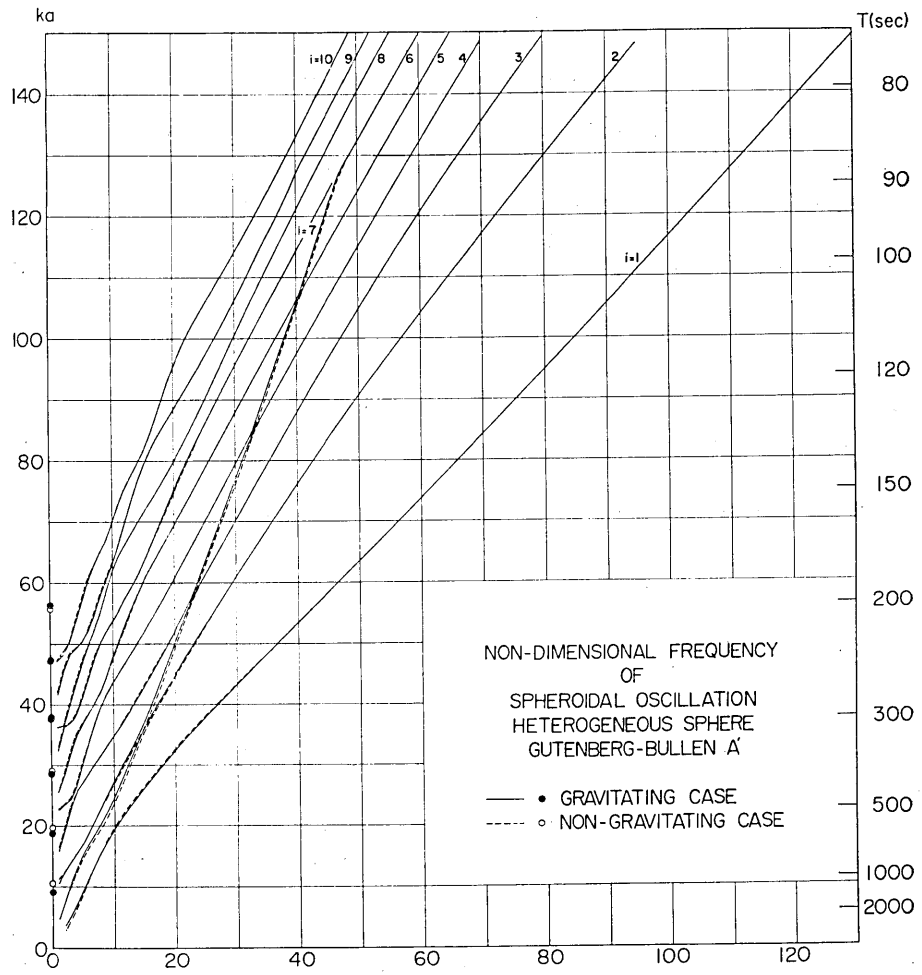

Figure 1a. Non-dimensional frequency ($\eta=ka=(2\pi a/V_{S0})/T$) of free spheroidal oscillations for the Gutenberg-Bullen A′ earth model. Solid curves and solid circles refer to the gravitating case and broken curves and open circles to the case without gravity.

Figure 1a appears in enlarged form as Figure 1b. These figures show that the discrepancy of non-dimensional frequency between cases (I) and (II) becomes smaller as the order number n increases. A noteworthy feature is the large difference in frequency along the transition segments between radial modes. Free spheroidal oscillations in these portions of the diagram are characterized by large amplitudes near the core-mantle boundary and the corresponding disturbances greatly resemble Stoneley-

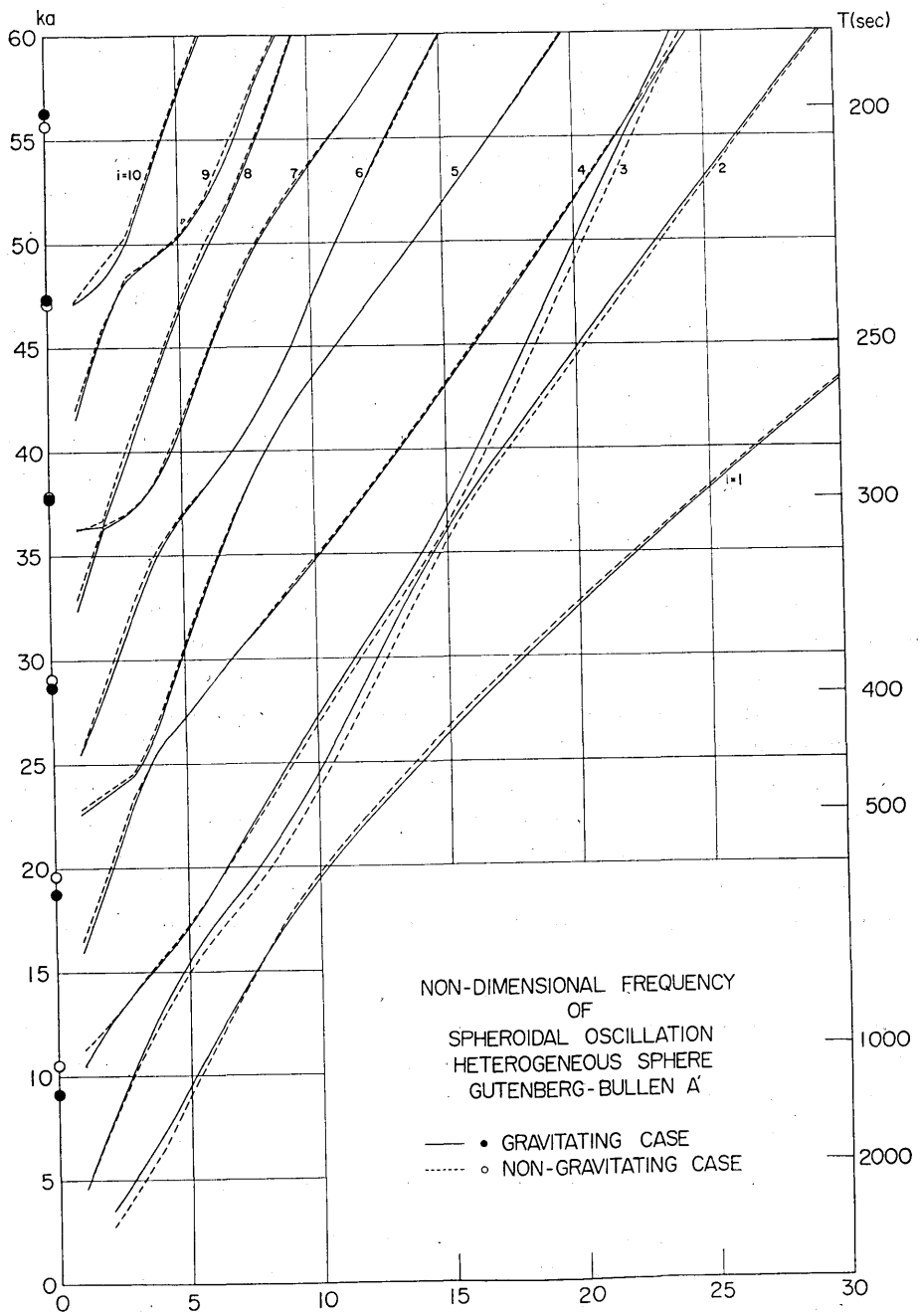

Figure 1b. Enlargement of a part of Figure 1a to illustrate some of the details for small values of the colatitudinal order number n.

wave propagation along the fluid-solid interface. Along these segments, the frequencies for case (II) are larger than those for case (I) and the difference is nearly constant.

When $n=0$, which corresponds to simple expansion and contraction of the earth, the introduction of gravity is accompanied by a decrease in frequency for the low order purely radial modes and an increase in frequency for the higher radial modes. By comparison, the introduction of gravity in the problem of the homogeneous elastic sphere[1] is accompanied by a decrease in frequency, which effect diminishes with increasing radial mode number i.

For the fundamental mode, $i=1$, the introduction of gravity is associated with an increase in the frequency of the graver orders of vibration for the present realistic earth model and for the homogeneous elastic sphere[1]. The increase in frequency diminishes in both cases for larger values of the order number n with, however, an important distinction. The frequency increase associated with the introduction of gravity decreases monotonically with order number for the homogeneous sphere. By contrast, the realistic model shows that the effect of gravity on fundamental mode frequencies reverses sign in the vicinity of orders $n=$ 7 and 8 and, after a fairly smooth excursion, gradually diminishes with increasing order number.

For the higher modes, $i>1$, the introduction of gravity is accompanied by a complicated pattern of frequency increases and decreases as a function of order number n and radial mode number i. As previously noted, the largest of these frequency changes is often associated with the regions of transition which are equivalent to Stoneley-wave propagation along the core boundary.

Comparison of Figures 1a and 1b with the corresponding illustrations for the homogeneous elastic sphere[1] indicates that the effect of gravity on the frequency of the spheroidal oscillations is greatly influenced by the physical properties of the earth model.

6. Radial Distribution of Displacement

The radial distribution of the radial and colatitudinal displacement for cases (I) and (II) is presented in Figure 2 for radial modes $i=1\sim4$ for the orders $n=1$, 2, 5, 10 and 15. The thick line represents the present result and the thin line corresponds to the non-gravitating case. The solid and broken lines indicate the radial and colatitudinal

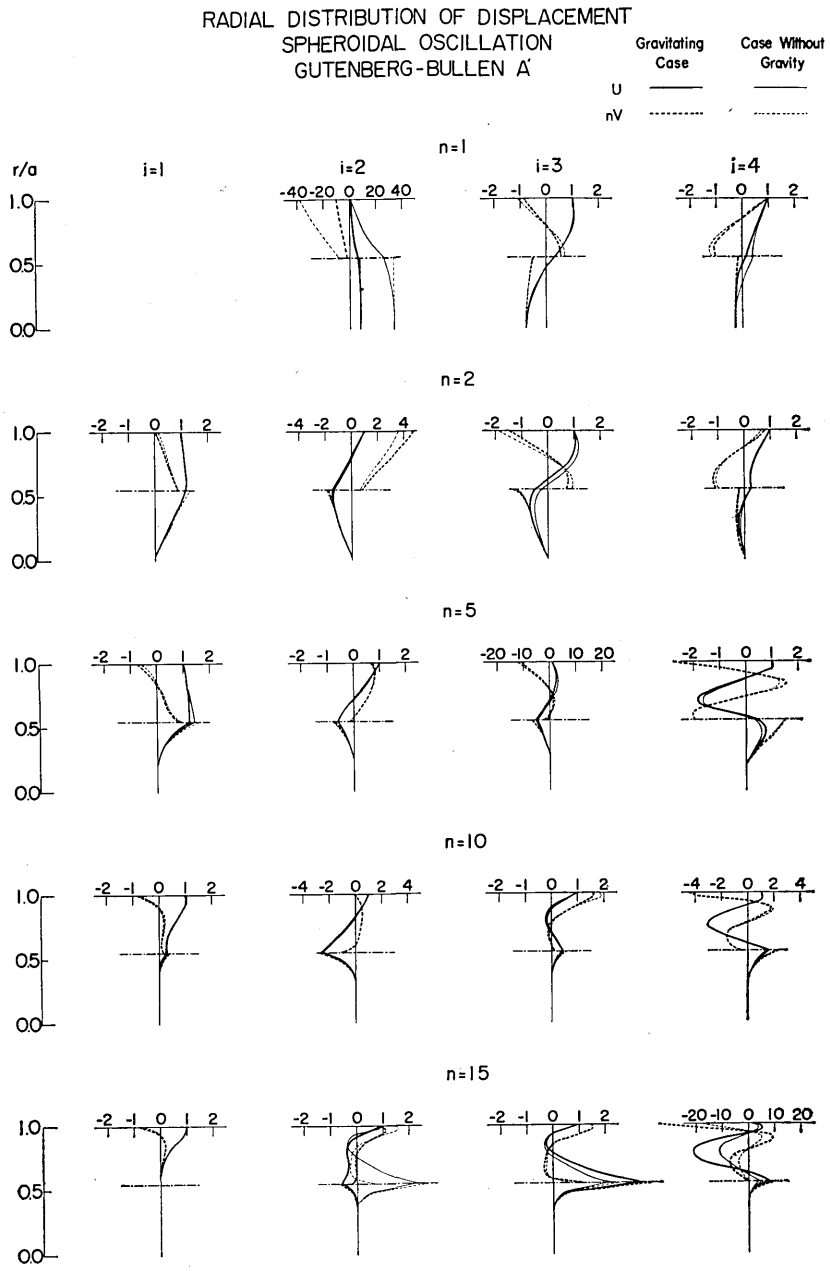

Figure 2. Radial distributions of the radial and colatitudinal components of displacement. The thick curves refer to the gravitating case and the thin curves to the case without gravity. Solid lines — radial component, broken lines — colatitudinal component. Chain lines indicate core-mantle boundary. Radial displacement taken equal to unity at the free surface.

components, respectively. All results have been normalized so that the radial displacement of the surface is one. When $n=1$, the center of the sphere oscillates along the polar axis.

The introduction of gravity is not, in general, accompanied by great changes in the distributions of displacement. The mode $i=2$ and $n=15$, however, exhibits a remarkable change, especially near the core boundary. Referring to Figure 1b, it may be noted that the introduction of gravity has caused this mode to migrate from the end of the transition segment to the beginning of the ordinary segment occupied by the higher orders when $i=2$.

The displacement distributions for the modes of transition segments, for example those of ($i=2$, $n=10$), ($i=2$, $n=15$), show large amplitudes near the core-mantle boundary, which is a characteristic feature of the Stoneley-wave along a boundary of two different elastic media.

7. Phase and Group Velocities

Phase and group velocities may be calculated from the non-dimensional frequency by means of the asymptotic formulae

$$C=V_{so}\cdot\eta/(n+1/2) \tag{7.1}$$

Table 1. Phase and group velocities for the Gutenberg-Bullen A′ earth model when the gravitational effect is considered.

	C (Phase Velocity) km/sec.					U (Group Velocity) km/sec.		
T(sec.) \ i	1	2	3	4	5	1	2	3
100	4.12	5.95	7.19	8.12	9.05	3.8_4	4.5_5	5.6_0
130				8.91	9.03			
200	4.60	7.23	8.68	8.80	11.06	3.5_8	5.6_6	
300	5.31	8.19	8.51	10.87		3.8_1	6.3_7	8.5_4
340								6.7_5
360							8.6_6	
400	5.29	8.29	9.11			4.4_1	8.5_4	6.8_9
500	6.36	8.37	9.77			4.9_5	7.3_0	7.4_2
600	6.62	8.93	10.44			5.8_1	5.4_8	7.1_0
650							5.5_0	
700	6.68	9.88	11.82			6.8_4	6.0_4	5.3_8
800	6.61	10.34				7.5_0	8.1_8	
900	6.50	10.61				7.8_1		
1000	6.37	10.76						

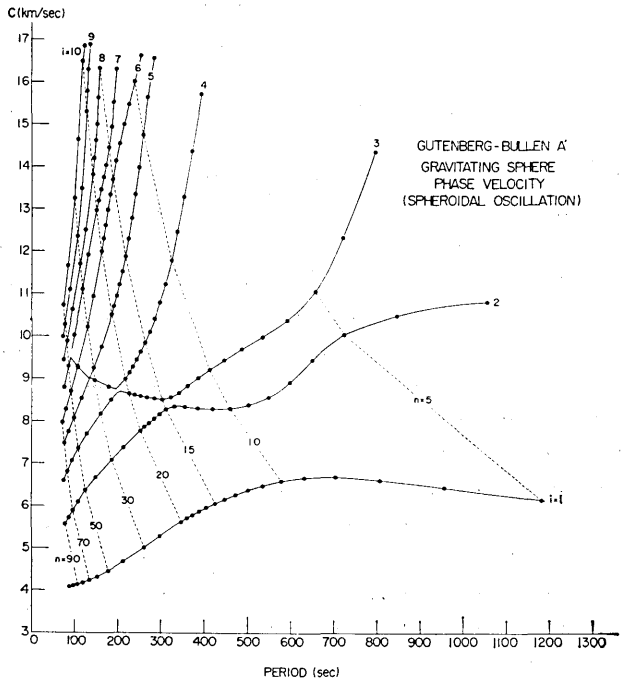

a

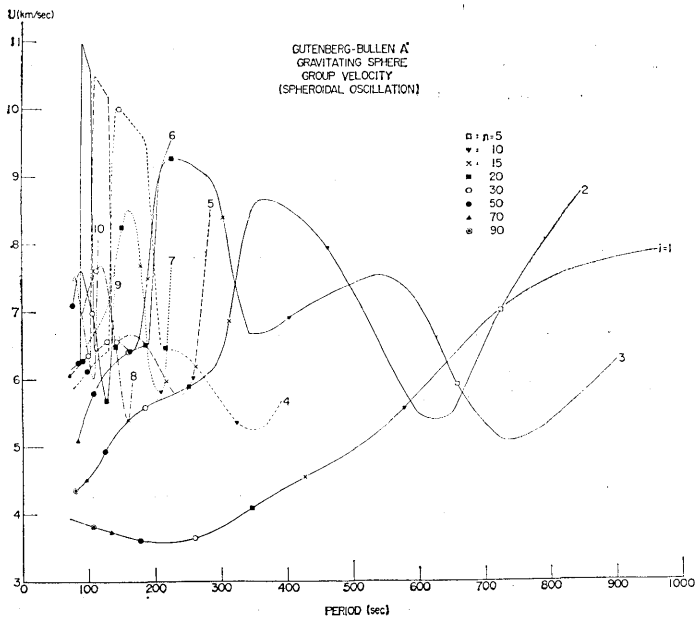

b

Figure 3. Phase and group velocity as functions of period for the radial modes $i=1\sim10$.

and $$U = V_{SO} \cdot d\eta/dn \ . \tag{7.2}$$

Graphical results are presented in Figures 3a and 3b and numerical values at several representative periods are given in Table 1, which may be compared to Table 2 of the non-gravitating case[4].

Since the phase and group velocities are related to the frequency η by the simple expressions above, the entire pattern exhibited by the frequencies for these two cases is projected in the corresponding phase and group velocity curves. Differences in phase and group velocity associated with introduction of gravity are large for modes on the transition segments and are especially evident for the graver orders of the first three radial modes.

The introduction of gravity alters the group velocity of the fundamental mode at long periods, but the velocity and period of the Airy phase minimum is not significantly changed. The maximum group velocity near 500 seconds for the radial mode $i=3$, associated with the R_h wave[4], becomes larger with the introduction of gravity. The group velocities of the higher modes exhibit well-developed narrow maxima for modes on the transition segments.

8. Common Spectrum

The common spectrum of the radial and colatitudinal components of displacement is defined to be

$$\left.\begin{aligned} {}_iS_n^u &= \left(\frac{S_{mn}}{dE_S/dp} + \frac{T_{mn}}{dE_T/dp}\right) \cdot U_n(r) \cdot f^*(p) \ , \\ {}_iS_n^v &= \left(\frac{S_{mn}}{dE_S/dp} + \frac{T_{mn}}{dE_T/dp}\right) \cdot V_n(r) \cdot f^*(p) \ . \end{aligned}\right\} \tag{8.1}$$

Using these expressions, equations (3.12) may be reduced to

$$\left.\begin{aligned} u(t) &= \frac{j}{2} \sum_{i,m,n} {}_iS_n^u \cdot P_n^m(\cos\theta) \cdot \begin{matrix}\cos \\ \sin\end{matrix} m\varphi \cdot \exp(jpt) \ , \\ v(t) &= \frac{j}{2} \sum_{i,m,n} {}_iS_n^v \cdot \frac{d}{d\theta} P_n^m(\cos\theta) \cdot \begin{matrix}\cos \\ \sin\end{matrix} m\varphi \cdot \exp(jpt) \ , \\ w(t) &= \frac{j}{2} \sum_{i,m,n} {}_iS_n^v \cdot \frac{mP_n^m(\cos\theta)}{\sin\theta} \cdot \begin{matrix}-\sin \\ \cos\end{matrix} m\varphi \cdot \exp(jpt) \ . \end{aligned}\right\} \tag{8.2}$$

Since the common spectrum $\{{}_iS_n^u, {}_iS_n^v\}$ is independent of the variables

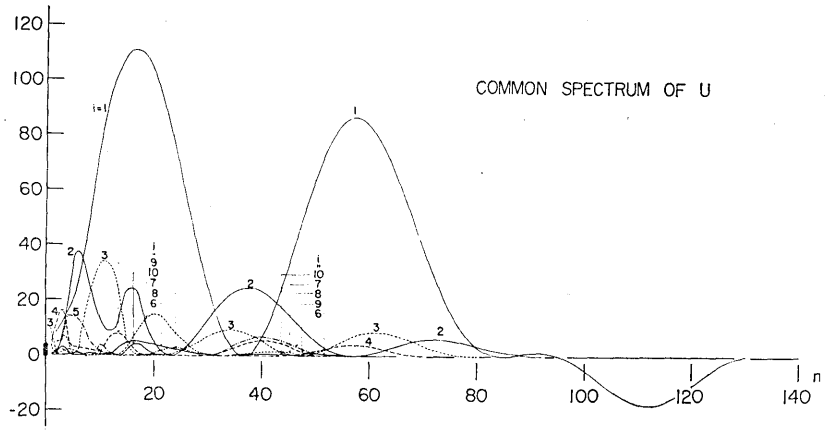

a

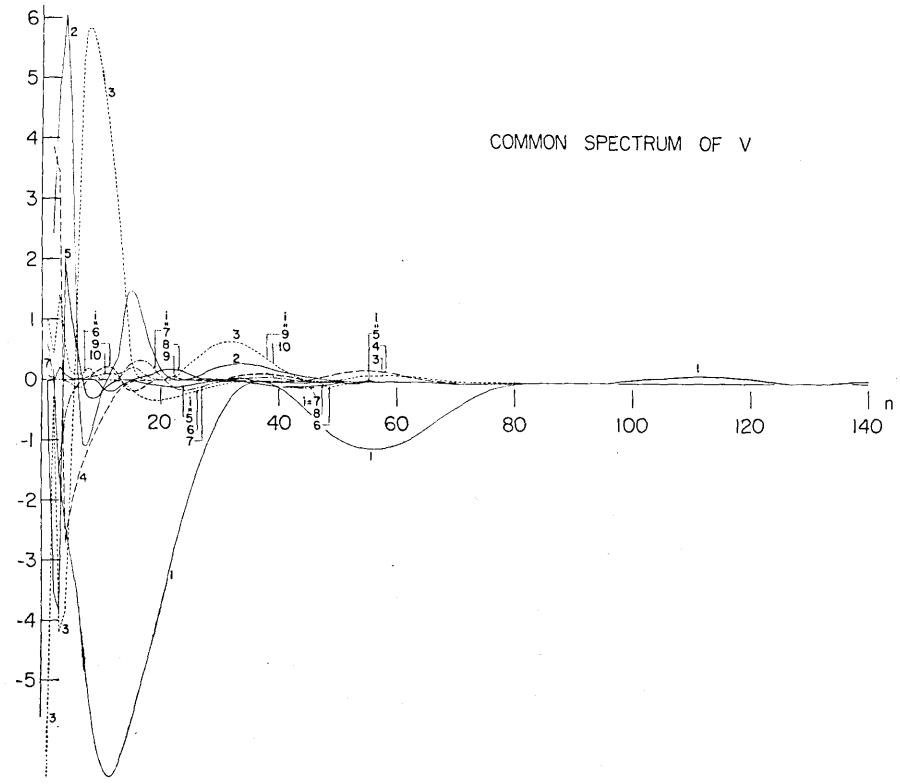

b

Figure 4. Common Spectrum of radial and colatitudinal components of displacement. Values of the radial component for purely radial oscillations ($n=0$) given by solid circles.

t, θ and φ, it may be used to calculate the displacement at all times and locations.

The radial and colatitudinal components of the common spectrum are shown in Figures 4a and 4b. The dots in Figure 4a refer to the values for the purely radial oscillations, $n=0$. Negligibly small values have been omitted from the figures in the interest of clarity.

The common spectrum becomes extremely small for modes lying along the transition segments discussed in section 5. Comparison of the common spectrum in the present study with that found for the non-gravitating case shows that:

1) In general, the results are quite similar for the two cases.

2) The introduction of gravity is associated, for $i=1$ and 2, with a decrease of the largest values of the radial component of the common spectrum and an increase of the corresponding colatitudinal component.

9. Theoretical Seismograms

A purely radial stress was assumed to be applied at the surface in a small circle around the pole, implying axial symmetry ($m=0$). Its spatial distribution is

$$\Phi(\theta, \varphi)=\Phi^0(\cos\theta)=\begin{cases}1 & \theta<\theta_0\\ 0 & \theta_0<\theta\end{cases} \quad (\theta_0=0.04 \text{ radian}) \tag{9.1}$$

The time function was taken to be

$$f(t)=\begin{cases}-1 & -t_1<t<0\\ 1 & 0<t<t_1\\ 0 & t_1<|t|\end{cases} \quad (t_1=0.02) \tag{9.2}$$

The Fourier transform of the function $f(t)$ is

$$f^*(p)=-4j\sin^2(pt_1/2)/p \tag{9.3}$$

The largest values of colatitudinal order number n employed in the synthesis may be inferred from the curves in Figure 4. Beyond these values, the spectral amplitudes are small and contributions from these modes were considered to be negligible.

Theoretical seismograms were calculated at three points on the surface, namely $\theta=30°$, 90° and 150° for the time interval $t=0.005(0.005)2.00$, and at eight points $\theta=15°$, 45°, 60°, 75°, 105°, 120°, 135° and 165° for

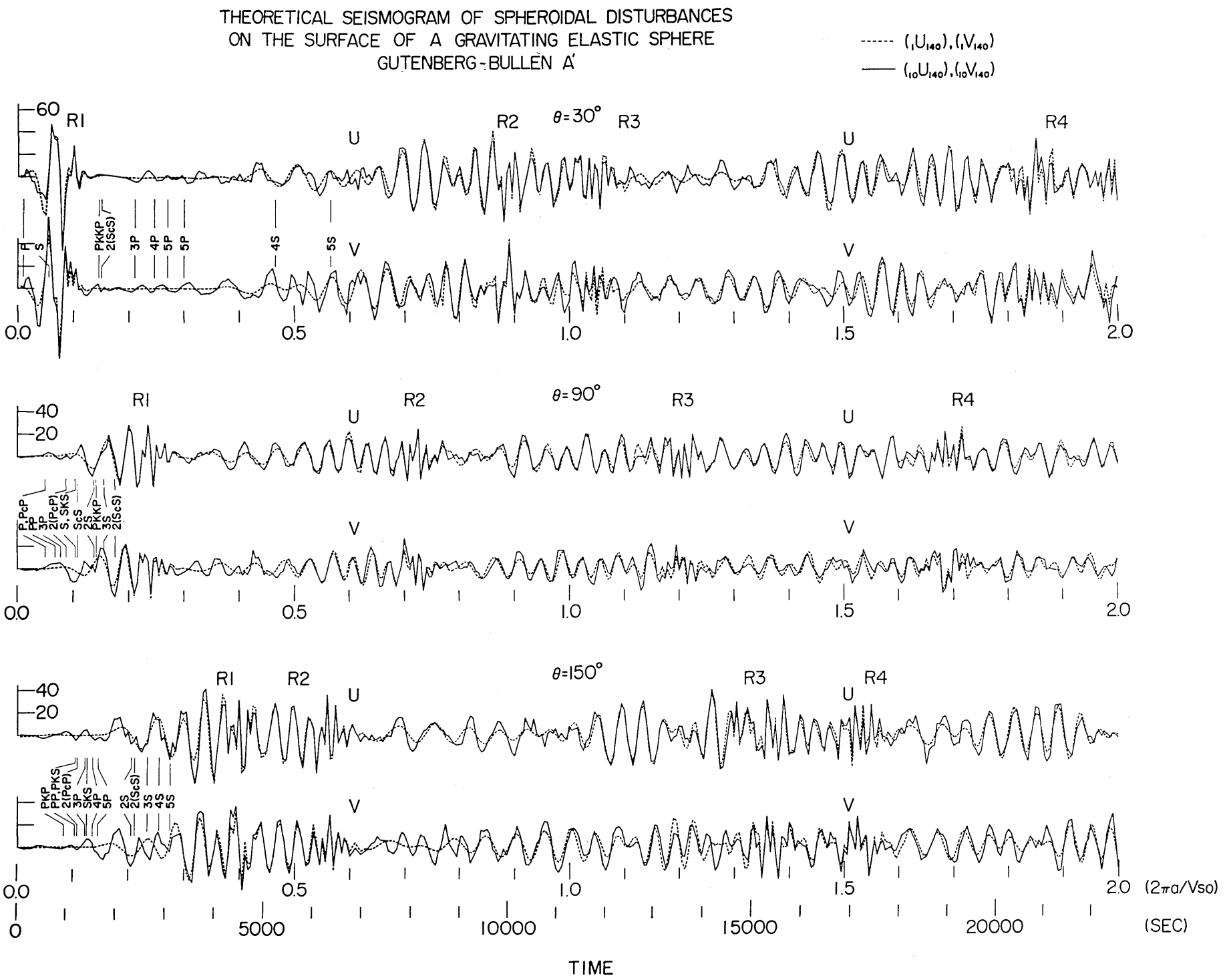

Figure 5. Theoretical seismograms of spheroidal disturbances on the surface of a Gutenberg-Bullen A′ earth model when the gravitational effect is considered. The external force is taken to be a uniform radial stress acting on a circular area around the pole. Solid lines $-({}_{10}u_{140})$ and $({}_{10}v_{140})$, broken lines $-({}_{1}u_{140})$ and $({}_{1}v_{140})$. Arrows indicate arrival times expected for various body waves. Unit of time: (circumference of the earth)/(surface shear velocity).

the time interval $t=0.005(0.005)1.0$. They are shown in Figures 5 and 6. $2\pi a/V_{S0}$, the time required for a shear wave to circle the globe, is taken as the unit of time.

In figure 5, the solid lines refer to $({}_{10}u_{140})$ and $({}_{10}v_{140})$ and the broken lines to $({}_{1}u_{140})$ and $({}_{1}v_{140})$. The arrows show the expected times of arrival for various body wave phases as predicted by geometrical optics. The agreement between the expected times of arrival and the actual times of appearance of the phases is satisfactory. The travel time curves of these phases for the present earth model were presented in Figure 6 of our previous paper[4].

Comparison of Figure 5 with the corresponding illustration for case (I), Figure 2, reveals that the results for the cases with and without gravity are quite similar shortly after the time of application of the external force. The difference between these two cases increases continuously, however, with the passage of time and becomes increasingly obvious, especially for the body wave arrivals (solid lines).

These theoretical seismograms realistically reproduce much of the character of the long period arrivals that are observed on actual teleseismic recordings. Figure 5 reveals the presence of the direct compressional and shear arrivals, phases reflected from the core and the free surface, as well as waves which have been transmitted through and refracted by the core. The Rayleigh waves end abruptly at travel times corresponding to the minimum group velocity of the fundamental mode, $U_{\min}=3.57$ km/sec, which is found for periods near 220 seconds. This illustration confirms that, as in case (I), the fundamental mode is primarily related to the surface waves and the higher modes correspond to the body waves. These body waves may be more clearly identified in the theoretical seismograms shown in Figure 6, which is a summation of only the higher radial modes ($i>1$).

The high velocity higher mode wave designated R_h, which is an outstanding feature of the seismograms in Figure 6, is associated as in case (I) with the Airy phase produced by the group velocity maximum of the radial mode $i=3$, for periods near 500 seconds[4]. The amplitude of this wave increases near the pole and the antipode, as is characteristic of surface waves on a sphere. The inclusion of gravity is accompanied by earlier arrival times for the main part of the R_h wave; Figure 6 shows that this difference increases with the passage of time.

The onset of the R_h wave in case (I) (without gravity) is especially clear for epicentral distances between 15° and 45°. The onset of the

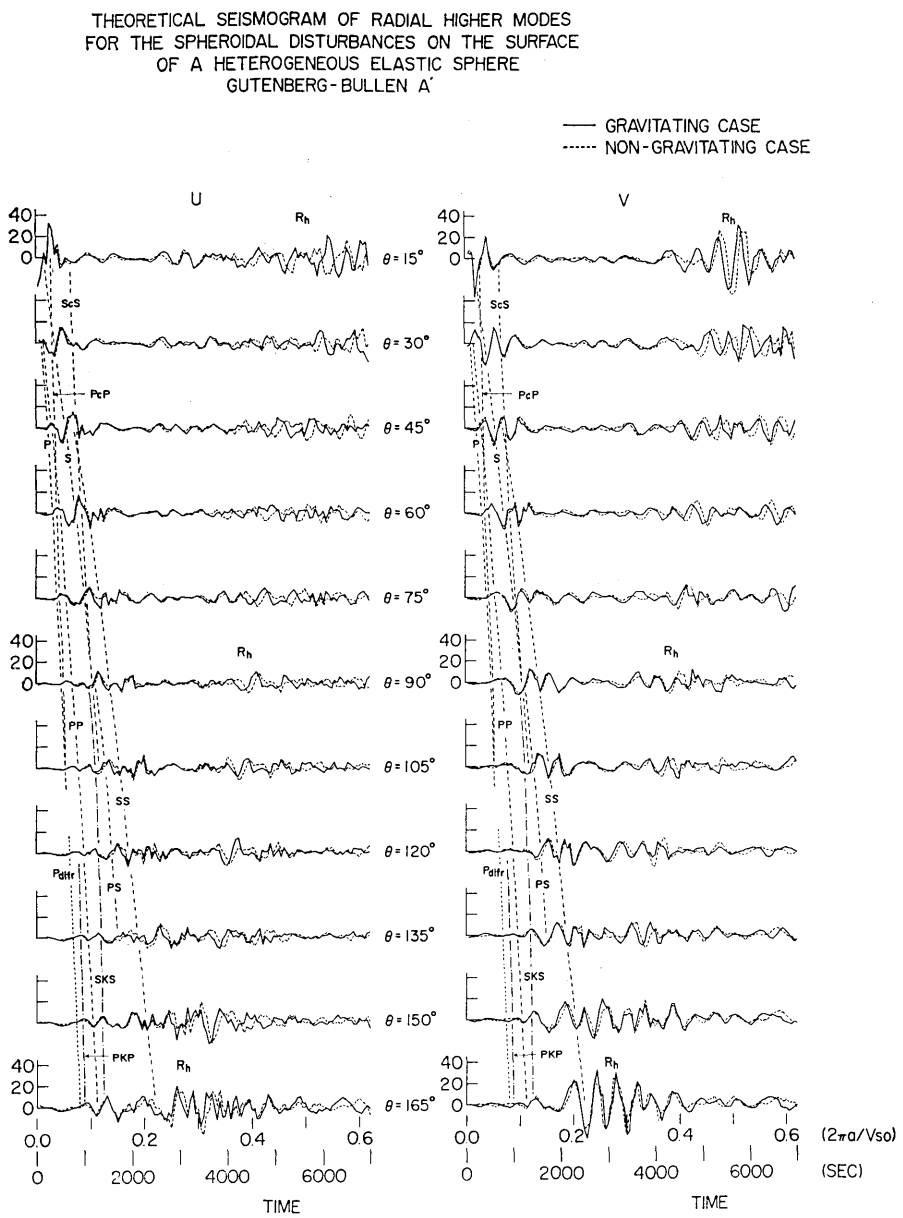

Figure 6. Theoretical seismograms consisting only of higher radial modes. Curves of travel time versus distance for various body waves are indicated by appropriate labels for broken and chain lines. Solid line and broken line seismograms refer to gravitating and non-gravitating cases respectively. Notation and time unit as in Figure 5.

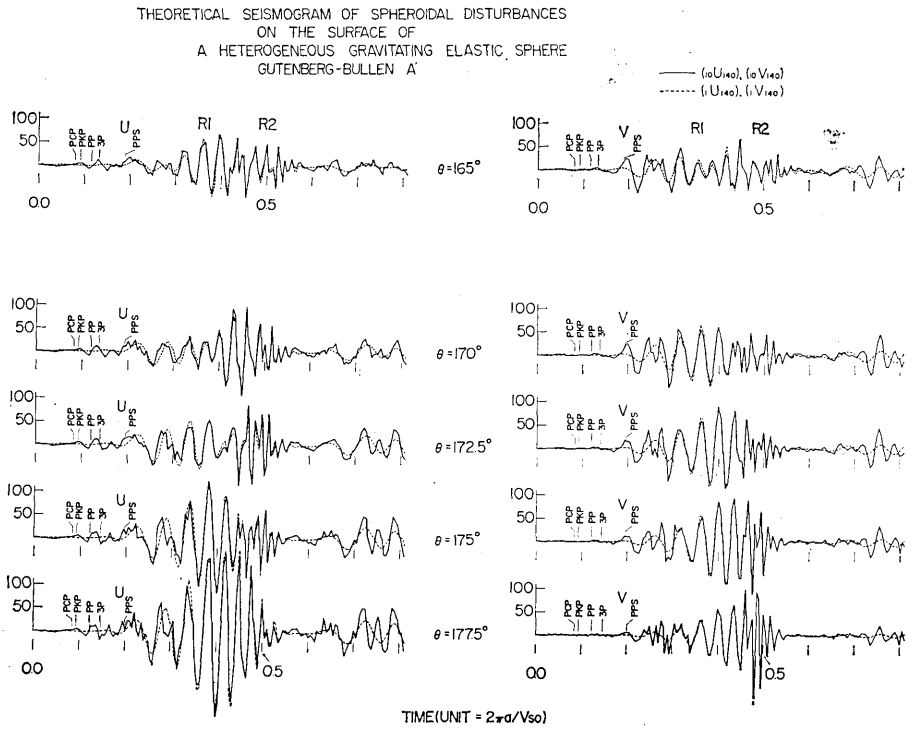

Figure 7. Theoretical seismograms illustrating the changing wave patterns near the antipode. Notation and time unit as in Figure 5.

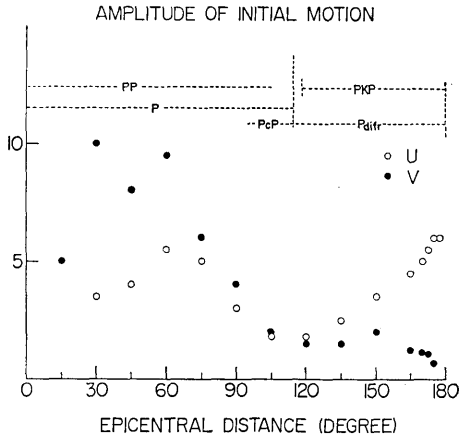

Figure 8. Amplitude of initial wave as a function of epicentral distance. Solid circles — colatitudinal displacement, open circles — radial displacement. First arriving body wave phases identified by name.

R_h wave, previously associated with the higher radial mode $i=2$[4], occurs earlier for case (II) (with gravity), an observation consistent with the higher group velocities found for case (II) in the vicinity of the corresponding group velocity maximum near 400 seconds. The correlation of the onset of the R_h wave with the higher radial mode $i=2$ may receive further support from the observed increase in colatitudinal amplitudes for case (II) (Figure 6). This observed increase is concordant with the larger values of the colatitudinal component of the common spectrum previously noted in the discussion of case (II) in section 8.

Figure 7 illustrates the gradual change in the wave pattern as the observation point approaches the antipode. The body phases which have spent all or almost all of their travel time as compressional waves begin to predominate as the antipode is approached. This observation, based on travel times, is supported by the increase in radial amplitudes and coincident decrease in colatitudinal amplitudes of the body phases for seismograms near the antipode in Figure 7. These results may also be seen in the plot of radial and colatitudinal components of body wave amplitude as functions of epicentral distance, presented in Figure 8.

The predominance of short period Rayleigh waves near the antipode may also be noted from the seismograms in Figure 7. This increase of Rayleigh wave amplitudes is an essential characteristic of surface wave propagation on a sphere.

Acknowledgements

The authors are greatly indebted to Professor Max Goldstein, Director of the computing laboratory of the Courant Institute of Mathematical Sciences, New York University, for his generous hospitality and provision of computing facilities, under the auspices of U. S. Atomic Energy Commission contract AT-(30-1)-14800. Additional parts of the computation were done through the project UNICON, and at the Computer Centre of the University of Tokyo, to all of whom our sincere thanks are due.

The authors are grateful to the Geosciences Division of the Southwest Center for Advanced Studies and the Earthquake Research Institute of the University of Tokyo for their help in arranging a visit of T. Usami to the former institution while on leave from the latter during the period of this study.

This cooperative research in the field of seismology was supported in part by the Japan Society for the Promotion of Science and the

National Science Foundation under grants Chi-26 and GF-237, respectively, as part of the Japan-U. S. Cooperative Science Program. This investigation was also supported by the National Scicnce Foundation under grants GP-5544 and GA-830, by the National Aeronautics and Space Administration, under contract NsG-269-62 with the Southwest Center for Advanced Studies and by supplemental research funds of the latter institution.

---

33. 重力均衡下にある弾性球の表面を伝わるスフェロイド型振動 II. グーテンベルグ・ブレン A′ モデルの場合

地震研究所 佐藤泰夫 宇佐美龍夫

Southwest Center for Advanced Studies Mark LANDISMAN

1. 筆者らは弾性球を伝わる擾乱の理論地震記象の研究をつづけてきた．前回には等質等方弾性球について，重力の影響を考慮した場合の計算を行なつた．今回は重力均衡下にある現実的な地球モデルの表面を伝わるスフェロイド型擾乱についてしらべた．方法は従来と同じで，変位を自由振動のいろいろなモードの和として表わした．

2. 地球モデルとしては前報と同じものを採用した．すなわち P 波，S 波の速度分布はグーテンベルグ，密度分布はブレン A′ を使つた．

3. まず，スフェロイド型の自由振動の周波数を $n=0(1)140$, $i=1(1)10$ の各モードについて計算した．重力がない場合の周波数と比べると，その差は周期の長いモードに大きく，とくに前報で述べた，ある高調波モードから次の高調波に移る遷移分枝上で著しく，この遷移分枝上では両者の周波数の差はほぼ一定である．また，周期が小さくなると，重力の影響は小さくなる．重力の影響は複雑でモードによつて異なる．また，等質等方弾性球に対する重力の影響を参照すると，重力の影響は，採用する地球モデルにより左右されることがわかる．

4. 表面における半径方向の振幅を単位として，おもなモードについて半径方向の振幅分布を図示した．重力の影響は一般には大きくない．しかし，重力を入れたために，性質の異なる分枝（第1図の周波数と n のグラフで）に移るモード（$i=2$, $n=15$）については，振幅分布の様子は大幅に変化する．

5. 重力の群速度と位相速度に及ぼす影響は周波数に対する影響を強く反映して $i=1\sim3$ のモードのうち n の小さいものに対して大きい．基準振動の極小群速度に相当する周期と群速度の値は重力の有無にほとんど影響されない．

6. また，スペクトルのうち，観測点の位置と時刻に無関係な部分をコモン・スペクトルと名づけ，いろいろな i に対し n の函数として図示した．その極大・極少値に及ぼす重力の影響はたかだか15% くらいである．

7. 実際の計算に当り，軸対称（$m=0$）を仮定した．外力としては極のまわりに次のような半径方向の力が働くとした．

$$\Phi(\theta,\varphi)=\Phi^0(\cos\theta)=\begin{cases}1 & \theta<\theta_0\\ 0 & \theta_0<\theta\end{cases}\quad(\theta_0=0.04\ \text{ラヂアン})$$

$$f(t)=\begin{cases}-1 & -t_1<t<0\\ 1 & 0<t<t_1\\ 0 & t_1<|t|\end{cases}\quad(t_1=0.02)$$

時間の単位しては(周長)/(地表の S 波速度)=11268 秒をとり,地球上の数点で時刻 $t=0.005(0.005)2.0$ について理論地震記象を計算した.

8. 計算の結果,次のことが明らかになつた.

a) 計算から求めた初動の走時は,理論地震記象に見られる発現時と一致する.

b) 核の陰での回折波が,高調波だけの和よりなる理論地震記象によく表われている.

c) 理論地震記象は,発震後の経過時間が少ないうちは,重力を無視した場合とよく似ているが,時間が経つとともに,違いが目立つてくる.その違いは実体波の部分に大きい.

d) 基準振動は表面波をよく表わしている.また高次の振動は実体波と関係している.重力のない場合と同様に,高次の振動からなる理論地震記象に,R_h 波と名づけた表面波の性質をもつた波が見られる.この波は主として $i=2$, 3 の周期 300～500 秒付近の極大・極少群速度に関係しているが,その群速度に対する重力の影響(第1表参照)を反映して,重力のない場合より少し早く表われる.とくに v 成分では両者の位相の差が見事に理論地震記象に見られる.

e) 極の付近での波のパターンの変化をみるために,第8図を画いた.P 群の波については極の近くで半径方向の振幅が増え,表面に沿う成分の振幅がほとんど零になる.また極の近くで急に短周期波が明らかに表われる.

f) 群速度の極小値に対応し,短周期波に着目すると,表面波の終りの点がはつきり理論地震記象に見出される.

9. 初動の振幅を震源距離の函数として示した.